Validation of the Circular Harmonic Transform (CHT) Algorithm for Quantitative SPECT

William G. Hawkins, Nai-Chuen Yang, and Peter K. Leichner

The Johns Hopkins Oncology Center, Department of Radiation Oncology, Johns Hopkins Medical Institutions, Baltimore, Maryland

The purpose of this study was to validate the use of the circular harmonic transform (CHT) algorithm for quantitative single-photon emission computed tomography (SPECT) with isotopes technetium-99m (^{99m}Tc) and indium-111 (^{111}In) under clinically relevant conditions. Phantom studies were the principal tools used. Volumes of fillable organs within a tissue-equivalent anthropomorphic phantom were determined over a wide range (145-1960 ml) to within 6% by using a thresholding technique. Additionally, phantom studies with nonuniform activity distributions were made. These included a background of activity and hot as well as cold lesions. The hot lesion was computed to within 12% (^{111}In) and 7.7% (^{99m}Tc), and contrast in the cold lesion was ~70% for both isotopes. The CHT algorithm incorporates the energy-distance relation (EDR) which minimizes the degrading effects of attenuation, scatter, collimator blur and poor statistics.

J Nucl Med 1991; 32:141-150

Ⅰn this article, quantitation of nonuniform concentrations of radionuclides is demonstrated with a methodology that is clinically practical and relevant. Also, single-photon emission computed tomography (SPECT) protocols and reconstruction algorithms are outlined that have been developed by our group for the calculation of radionuclide concentration with sufficient accuracy to allow clinical application to diagnostic nuclear medicine studies and to quantitative radiolabeled antibody imaging in radioimmunotherapy.

In the development of such a protocol for SPECT based on planar gamma camera images, one is faced with several constraints: (1) type of equipment, (2) choice of algorithm, processing time, and (3) sensitivity, spatial resolution, and stability of the gamma camera.

These constraints are interrelated, but the interaction of (1) and (2) is particularly important.

We have developed a SPECT reconstruction algorithm, the circular harmonic transform (CHT) algorithm (*1*) that is noniterative, and strikes the right balance between complexity, computational requirements, quantitative accuracy and clinical relevance. We have used a microcomputer interfaced with an array processor to reconstruct SPECT data and to perform a variety of image processing tasks. The algorithm is relatively efficient, and requires on the order of M^3 floating-point operations for an M × M reconstruction, the same as filtered backprojection (*1,2*).

The CHT algorithm for SPECT is based on the analytic solution of the exponential radon transform within a convex boundary, and the Circular Harmonic Transform-Fourier Transform (CHT-FT) of the sinogram of the centered or premultiplied projection data (*1-4*).
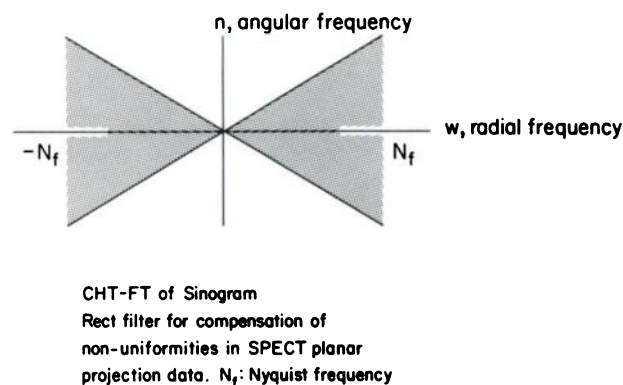
For SPECT with parallel-ray collimation, a generalized Hankel transform of the image was matched to the CHT-FT of the sinogram (*1,5*). This property allowed for the efficient and accurate calculation of the Hankel transform of the image without interpolation of the projection data. Backprojection, a convolution intergral in image or projection space is reduced to multiplication in frequency space. The generalized Hankel transform is directly inverted by the use of the FT to obtain image points evenly spaced on a polar grid. For display on a rectangular grid, interpolation or "image conversion" is required. The computational requirement for properly optimized image conversion is minimal, and does not require the use of the array processor.

Recent studies of the CHT-FT of the SPECT sinogram have demonstrated an important connection between the energy concentration of the signal and source-detector distance (*1,6*), the energy-distance relation (EDR) or frequency-distance relation. The EDR is based on stationary phase approximations of the two-dimensional complex exponential transform of the projection sinogram. The principle was first discovered by

Edholm et al. (6). The EDR was shown to be more general, and a stationary phase principle was found and applied to other tomographic geometries including SPECT (1). Although the EDR is based on a stationary phase approximation, it must be emphasized that the CHT solution for the exponential radon transform (1), which is fundamentally based on the EDR, is nonetheless an exact solution. The EDR is a new concept in tomography that offers new approaches to old problems (7).

The power spectrum of the CHT-FT of the sinogram easily separates into two distinct segments, one of which corresponds to the signal from each source pixel when it is in the near half-plane of the detector, and the other segment which corresponds to the signal from each source pixel when it is in the far half-plane of the detector (Fig. 1). By using the modulus of the near half-plane signal only, the root-mean-square (RMS) error of the resulting reconstruction is greatly improved, and the effects of attenuation, scatter, and collimator blur are minimized.

Earlier SPECT reconstruction methods often relied on the averaging of opposing views. This approach compensated for a number of deficiencies; counting statistics improved and the effects of camera nonuniformities were lessened. The use of the CHT algorithm does not preclude a variation of this technique, because the near half-plane signal and the far half-plane can be averaged in CHT-FT space. However, the EDR implies that neither type of averaging is optimal for SPECT reconstruction, since by averaging opposing views, one effectively dilutes the near half-plane signal with the far half-plane signal. The far half-plane signal is incorporated into the CHT algorithm, but it supplies only phase or positional information (1). By using the phase only of the far-field signal, we have retained some of the advantages of averaging opposing views while avoiding the most important disadvantage, the low signal-to-noise ratio of the far-field signal. One consequence of this approach is that the depth dependence of the image point response function for the CHT algorithm is less critical than with conventional SPECT, and the deconvolution parameters can be optimized for sources at moderate depth (2-5 cm within the attenuating medium). To realize the full advantage of this approach however, it is best to correct carefully for camera nonuniformities, camera resolving time (the near half-plane signal is differentially enhanced), and in many cases, correction for attenuation of the scanning table (see the Appendix for a derivation of the CHT algorithm based on EDR).

Any balanced approach must take into account the effects of scatter and collimator blur, as well as attenuation. For the minimal amount of scatter and collimator blur that are still present in the near half-plane signal, and to improve z-axis resolution, we have developed new image restoration software for planar projections, a non-linear Fourier statistical filter based on the Wiener and Metz filters (8-10). It is important to note that the effects of filtering and premultiplying are to enhance the near half-plane signal, as is shown in Figure 2. We have developed a new approach to the deconvolution of scatter and collimator blur from projections. The mathematical model that we use is a modified two-dimensional extension of the additive one-dimensional model of Floyd et al. (11).
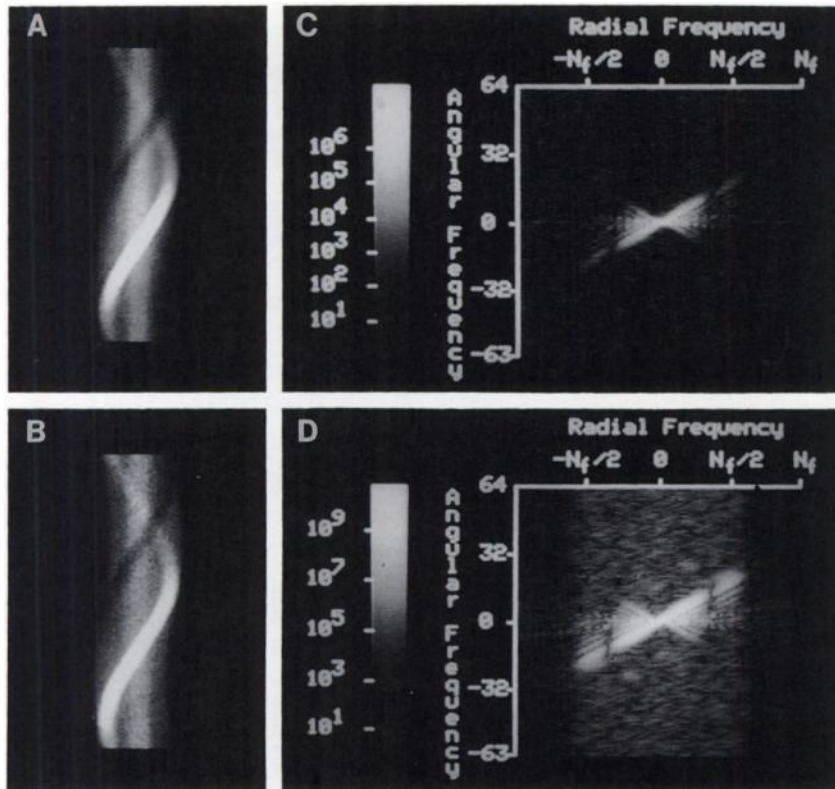
METHODS AND MATERIALS

The methodology required for CHT-SPECT consists of three general categories: (1) SPECT scanning protocol and quality control, (2) CHT reconstruction software and reconstruction protocol, and (3) tomographic calibration and phantom studies.

SPECT Scanning Protocol and Quality Control

A rotating gamma camera system with elliptical orbits was used to collect tomographic data sets of planar projections (GE 400AT, Milwaukee, WI). These data were uniformity-corrected on the vendor-supplied computing system (Data General Nova) interfaced to the gamma camera.

For the SPECT system used in this investigation, 128 views were acquired in a 360° rotation. To keep the image acquisition within a clinically acceptable limit of about 30 min, time per frame was set at 15 sec. Counts per frame need not be very high to optimize CHT-SPECT reconstruction. Total counts in the entire study have a greater effect on the RMS error than total counts per planar image. We begin to see a divergence between a planar image that is optimal for SPECT and one that is optimal for a planar study. The angular resolution of the SPECT reconstruction, as determined by the number of projection angles, N, must match or exceed the spatial resolution of the camera when the source point is close

CHT-FT of Sinogram
Rect filter for compensation of
non-uniformities in SPECT planar
projection data. N_f: Nyquist frequency

FIGURE 1
The signal energy of the CHT-FT of the SPECT sinogram is concentrated almost entirely within the bow-tie shaded region of the n-w plane. The upper right (n,w > 0) and lower left (n,w < 0) sectors are the near-field signal, and the lower right (n < 0, w > 0) and upper left (n > 0, w < 0) sectors are the far-field signal. The sectors are bounded by the lines $n = \pm \pi Dw$, where D is the diameter of the circle inscribing the patient's activity distribution. The rectangular nonuniformity filter is shown along the n = 0 axis.

FIGURE 2
Enhancement of near-field signal in CHT-FT of sinogram after planar image restoration filter and pre-multiply. (A) Sinogram of slice of Figure 5 before processing. (B) Sinogram after filtering and pre-multiply. (C) CHT-FT of (A). (D) CHT-FT of (B). Note enhancement of near-field signal in (D). The quantity N_f is the radial Nyquist frequency and is equal to one-half of the reciprocal of the linear pixel dimension.

to the camera. Because of the EDR, this consideration is even more important, since a given amount of linear displacement perpendicular to the camera face results in increasing angular displacement as the source point moves closer to the camera. If N is not sufficiently large, there will be angular undersampling of the near-field signal, and angular artifacts will be present in the reconstructions regardless of the total counts in the study.

For technetium-99m (^{99m}Tc) SPECT, a cobalt-57 (^{57}Co) sheet source was used for a uniformity correction. When a new ^{57}Co sheet source was received, it was mapped to determine any nonuniformities (12). If all image elements of the sheet source were uniform within 1%, the sheet source was used without a correction matrix. If the sheet source was not sufficiently uniform, or a high-count tomographic study was planned, the correction matrix was used for an additional uniformity correction.

For indium-111 (^{111}In), a fillable flood source was used. During the uniformity acquisition, the flood source was translated and rotated from its original position in order to average out slight variations in the thickness of the source.

In addition to these quality control procedures, the SPECT system was checked for spatial linearity and z-axis alignment. Calibration measurements such as center-of-rotation and sensitivity were performed routinely. Energy windows are 20% centered on the photopeak for ^{99m}Tc, and 10% centered on each photopeak of 173 KeV and 247 KeV for ^{111}In.

CHT Reconstruction Software and Protocol

A flow chart of the reconstruction process is given in Figure 3. All image processing and reconstructions were performed on a Microvax II (Maynard, MA) interfaced to a Sky Warrior

array processor (Sky Computers, Inc., Lowell, MA). The generation of an accurate body contour is an important part of the intrinsic algorithm. This process breaks down into two tasks: first, the generation of body edges from planar images, and, second, the reconstruction of the body contour from the body edges.

The generation of an accurate body edge from SPECT projection data depends on the nature of the radionuclide distribution. The most difficult cases are those for which the isotope distribution is focal, combined with poor statistics. In this case Compton scatter peak images are necessary and we use the method (13) to generate edges. When good statistics and a systemic distribution are present as in radiolabeled antibody imaging, the edges are obtained from primary peak images and the processing is much simpler. The contours are generated without having to reconstruct the SPECT slices. The edge coordinates are first corrected for center-of-rotation. From a 360° scan, edges from opposing views are averaged to reduce noise. Then the edges are mathematically backprojected to find the contour. The method is fast, and is based on geometrical backprojection of parallel edges.

All 128 sets of parallel edges are used, as well as the fact that a convex contour is generated by the intersection of strictly convex sets of parallel edges (points interior to pairs of parallel edges). A preliminary reconstruction to determine the boundary is not required, nor are pixel-filling or pixel-blocking techniques used. Contour-generation requires very little processing time.

Nonlinear Fourier Statistical Filter

We used a linear shift-invariant (LSI) model of scatter and collimator blur. The EDR minimizes, but does not completely

eliminate the shift-variant nature of these phenomena (7). Line sources are used to determine scatter full width at half-maximum (FWHM), scatter counts/total counts fraction, collimator FWHM and narrow-beam attenuation coefficient. The line source consisted of a 1mm i.d. pipette, 15 cm in length. It was mounted horizontally in a water bath and perpendicular to the optical axis of the gamma camera. Planar images were taken in the air, and in water at 1 cm increments from 1 to 5 cm, and then at 7.5, 10, 12.5, and 15 cm. The images were corrected for decay and camera resolving time. The broad-beam attenuation coefficient was calculated for parallel-hole collimators by summing over all counts in each image (14). A line source profile was created by summing cross-sections for which the line source profile was uniform, and a mathematical model was fitted to the profile by use of a standard nonlinear curve-fitting algorithm. Details of the line source model will be discussed in the section on tomographic calibration.

This model is used in conjunction with the two-dimensional Fourier statistical filter of the planar projections that differ in important ways from other applications of the Metz and Wiener filters (8). Since the Wiener filter is a nonlinear filter (the power spectrum of the object is required a priori in order to obtain an estimate of the object), estimating the object power spectrum is very important. Also, an object power spectrum with Hermetian symmetry only is used, in contrast with other approaches that use a radially averaged object power spectrum.

Investigations into the image power spectrum of planar projection data have allowed us to include decay corrections and camera resolving time corrections in the Fourier statistical model. Thus, we have developed a two-dimensional Fourier statistical filter that is image-dependent and count-dependent.

The filter has also been implemented on the array processor, and filtering of a 64 × 64 image requires only 1.2 sec. This filter is used for quantitative SPECT and was used to reconstruct the transverse slices for the nonuniform activity phantom.

Pre-multiply Algorithm

The pre-multiply step is contour-dependent and must be done separately for each planar view in the intrinsic method. As shown in Figure 3, it is the first step in the CHT reconstruction algorithm. It is also referred to as the centering of the projection data, because this mathematical operation removes the effect of the contour. A set of smooth, noise-free contours is important because the pre-multiply step usually "boosts" the signal so that on the average, any noise gets amplified. The convex contour is stored as a 128-point polygon, and a first order interpolation method based on polygon segment driven logic is used to determine the intersection of the projection ray with the polygon. Once the pre-multiply factors and table correction factors have been determined, the array processor is used to complete this computational step. Also, the CHT-FT of the sinogram may be filtered for further uniformity compensation (15). Because nonuniformities manifest themselves as vertical streaks in the sinogram, they appear mostly in the zeroth angular harmonic, high radial frequency region of the CHT-FT of the sinogram. A simple rectangular filter that removes these frequencies affords some additional compensation for nonuniformities. As is shown in
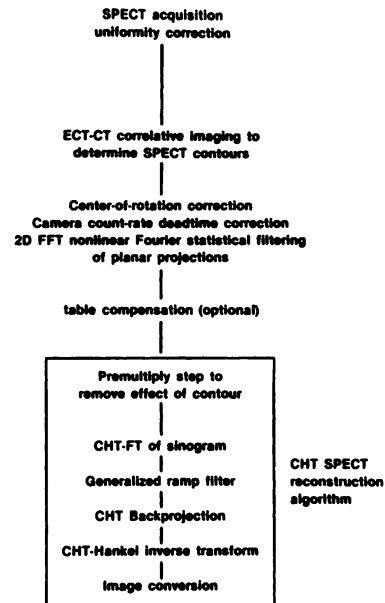

FIGURE 3
Flow chart of CHT SPECT reconstruction protocol.

Figure 2, the rect filter, rect(n,w) is specified by:

$$\text{rect}(n, w) = \begin{cases} 0, & n = 0 \text{ and } |w| > U_n \\ 1, & \text{otherwise,} \end{cases}$$

where U_n is a radial frequency supplied by the user. An option exists in the CHT reconstruction software to allow the user to specify the size of the rect filter.

The rest of the details for the implementation of the CHT-SPECT reconstruction algorithm can be found in Reference 1.

Tomographic Calibration and Phantom Studies

In this section, we shall outline the remaining measurements and procedures necessary to obtain meaningful regional or voxel quantitation.

Line sources are a practical and convenient means of obtaining information about scatter, collimator resolution, and the narrow-beam attenuation coefficient, but the function obtained from fitting the transverse cross-section of a line source is the one-dimensional projection or radon transform of the corresponding radially symmetric two-dimensional function. If the finite length of the line source is neglected, the one-dimensional Fourier transform of a transverse section of a line-source function is the zeroth order Hankel transform of the two-dimensional point response function (16). For example, if the line source data are fitted to:

$$Ag(x:\sigma) + Bk(x:\beta) \qquad \text{Eq. 1}$$

with

$$g(x; \sigma) = \exp(-x^2/\sigma^2)$$

and

$$k(x; \beta) = \exp(-\beta|x|)$$

then the two-dimensional point response function is a linear combination of $G(r:\sigma)$, a Gaussian function, and the modified

Bessel function $K_0(\beta|r|)$. The function $K_0(\beta|r|)$ has a log singularity at $r = 0$, but its two-dimensional Fourier transform is well-behaved, so frequency space deconvolution is possible. Image space deconvolution in two-dimensional space is also possible, because the log singularity of the K_0 function at $r = 0$ is removable, i.e., the value of K_0 at $r = 0$ can be replaced by a finite value for the purpose of calculating two-dimensional convolution integrals. However, this approach is not practical because K_0 is not sufficiently "concentrated" or point-like for optimized numerical convolution. This caveat also applies to SPECT point-source profiles in a scattering medium. The K_0 function is monoexponential in character for r bounded away from zero, and thus fits the two-dimensional response function well.

Determining the Gain Factor

For the ^{99m}Tc study, the gain factor was determined by using the known total activity in the phantom. For the ^{111}In study, the gain factor was determined by scanning a known uniform concentration of ^{111}In in a 500-cc plastic bottle. The uniform bottle study was reconstructed using the same reconstruction parameters that were determined to be optimal for the ^{111}In phantom study with nonuniform activities.

The calibration gain factor G_C was determined as follows: From the known concentration and cross-sectional area of the uniform phantom, the ROI software was used to generate ROIs of the same cross-sectional area from several representative slices of the reconstruction.

About 80% of the volume of the uniform phantom was incorporated into the ROI study for representative sampling. From this analysis, the calibration factor G_C in terms of $(\mu Ci/ml)/(counts/voxel)$ can be determined. Here, counts refers to image-pixel values, not photons. With the calibration sensitivity, we were able to determine gain factors for subsequent studies. From dimensional analysis, the gain factor, G_X can be determined from the equation;

$$G_x S_x t_x Z_c^3 C_x = G_c S_c t_c Z_x^3 C_c, \qquad \text{Eq. 2}$$

where

S_X, S_C are data set scale factors, t_x, t_c are time per frame [s] in the SPECT acquisitions, not including time for camera movement between frames, Z_x, Z_c are camera zoom factors, and C_x, C_c are sensitivity measurements in photon counts/$(\mu Ci\text{-sec})$. We assume that the isotope, matrix size, number of projection angles, collimator, and energy windows are not varied.

The meaning of the variables of Equation 2 are obvious except possibly for the scale factors. Image data on our system are represented as 16-bit integers. For all image processing and reconstruction work, the data are converted to 32-bit floating point representation, and all calculations are performed in floating point arithmetic. Intermediate results are converted to 16-bit integer format and stored on disk. In order to retain precision at each intermediate step, the floating point data are scaled before conversion to 16-bit integer form. This retains the numerical precision of the floating point calculation, without the increased storage that would be required for intermediate floating point results. The reconstructed image has a scale factor that is the product of successive scaling of intermediate results, and the scale factor may differ from study to study. The zoom factor Z_x may be different from Z_c,

but the sensitivity measurement C_x must be obtained with zoom factor Z_x, because sensitivity varies significantly with zoom factor. The input parameters to the Fourier statistical filter are FWHM of the collimator, scatter fraction, and FWHM of the scatter function. Scaling the FWHM parameters according to pixel size so that the physical dimensions remained invariant worked well, as long as the zoom factor was no larger than ~ 1.6 times the calibration zoom factor; camera resolution can significantly improve with large zoom factors. No additional line source measurements are needed for different zoom factors within this range.

SPECT Volume Computations

To test the capability of the CHT algorithm for SPECT volumetrics, a tissue equivalent anthropomorphic phantom with fillable organs was imaged. The organs were filled with a uniform concentration of ^{99m}Tc and each organ was scanned separately within the phantom. First, the global maximum for a particular organ was determined from all slices. Then a voxel was determined to be an organ voxel if it was above a certain percentage of the maximum. Using a least-squares fit to known volumes, we determined that a 33% threshold was optimal to minimize the error in volume determinations over the range and shapes of volumes studied.

Nonuniform Activity Distributions

To test the CHT algorithm and reconstruction software for hot and cold lesion detection in a uniform background of activity, we inserted three plastic containers in a commercially available SPECT phantom (Fig. 4).

The range of activities ($\mu Ci/ml$) was similar to the tumor-to-normal liver ratios of radiolabeled antiferritin in hepatoma patients (17,18) and care was taken to simulate patient studies as much as possible. Transverse slices were reconstructed using the CHT algorithm and software developed in-house and were
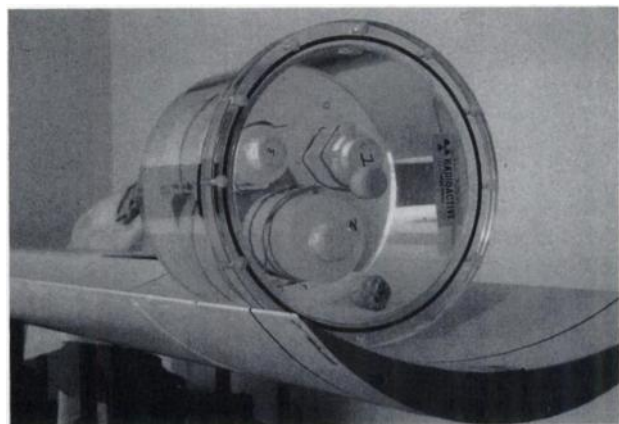
FIGURE 4
Photograph of phantom with nonuniform distribution of activities. Studies were performed with both ^{99m}Tc and ^{111}In. For ^{99m}Tc, the cylindrical phantom was filled with a uniform distribution, B = 1.28 $\mu Ci/ml$. Container No. 1 was filled with plain water (cold lesion) and had a diameter of 5.0 cm. Container No. 2 (diameter 7.2 cm) was filled with 3.85 $\mu Ci/ml$, and Container No. 3 (diameter 5.0 cm) was the hottest region and was filled with 8.0 $\mu Ci/ml$ activity. The ^{111}In study was similar except that concentrations and bottle placements were different (see Tables 2 and 3).

compared with transverse slices obtained with commercially available reconstruction software. Representative results are shown in Figure 5.

Determination of Regional Activity

Once a tomographic study was acquired and a gain factor determined, ROI software developed in-house was used to determine the activity within each region. The use of a phantom with cylindrical symmetry simplified the analysis. To determine the ROI, a thresholding method was used. For example, the cross-sectional area of bottle #2 in both nonuniform activity studies was 106 pixels. The threshold was selected to yield in this area, and the total counts in this ROI were converted to activity. The hot region and the medium region could be analyzed in this way.

To analyze the background region, we used a seed-pixel thresholding technique. With this method, a representative pixel within the ROI was selected. We used the cross-sectional area of the phantom to determine the lower threshold. In order to exclude regions of higher activity, an upper threshold, >100% of the magnitude of the seed pixel, was selected. This threshold was determined by subtracting out the areas of the hotter regions from the total area. Thus, all of the background pixels in a nonuniform slice were included in the ROI. The cold region required a different approach. First, the threshold for the hot region was determined. Since the hot region and the cold region were the same size, the ROI was moved until it was superimposed over the cold region, and the activity was measured. Thus the contrast for the cold region given above was very reasonable, because the ROI from which it was

determined was of the same cross-sectional area and shape as the 125 cc container. In all studies, images were acquired in 64 × 64 matrices.

## Clinical Comparison: CHT SPECT and Conjugate Planar Views

The conjugate view method for radionuclide quantitation has proven to be accurate and reliable for estimating total activity or activity in larger lesions in patients. The method utilizes a nonuniform attenuation correction based on a transmission image (19,20). The accuracy of this method for small, focal lesions is less than satisfactory and was one of the motivations for developing quantitative SPECT. In Figure 6, we show how ROI analysis was used to check the accuracy of CHT SPECT in a clinical study. The patient was given ^{111}In-antiferritin and both SPECT data and a conjugate planar view study were acquired. In Figure 6A, we show the ROI that was used to determine the activity in the tumor. In Figure 6B, we show the ROI that was used with the CHT SPECT transverse slices to simulate the ROI that would correspond to the conjugate planar view method. All transverse slices in which the lesion was present were analyzed in the same way. The results are given in Table 4.

RESULTS

The results of the volume determinations are summarized in Table 1. These demonstrate that in phantoms the agreement between actual and computated volumes is satisfactory. The transverse SPECT slices in
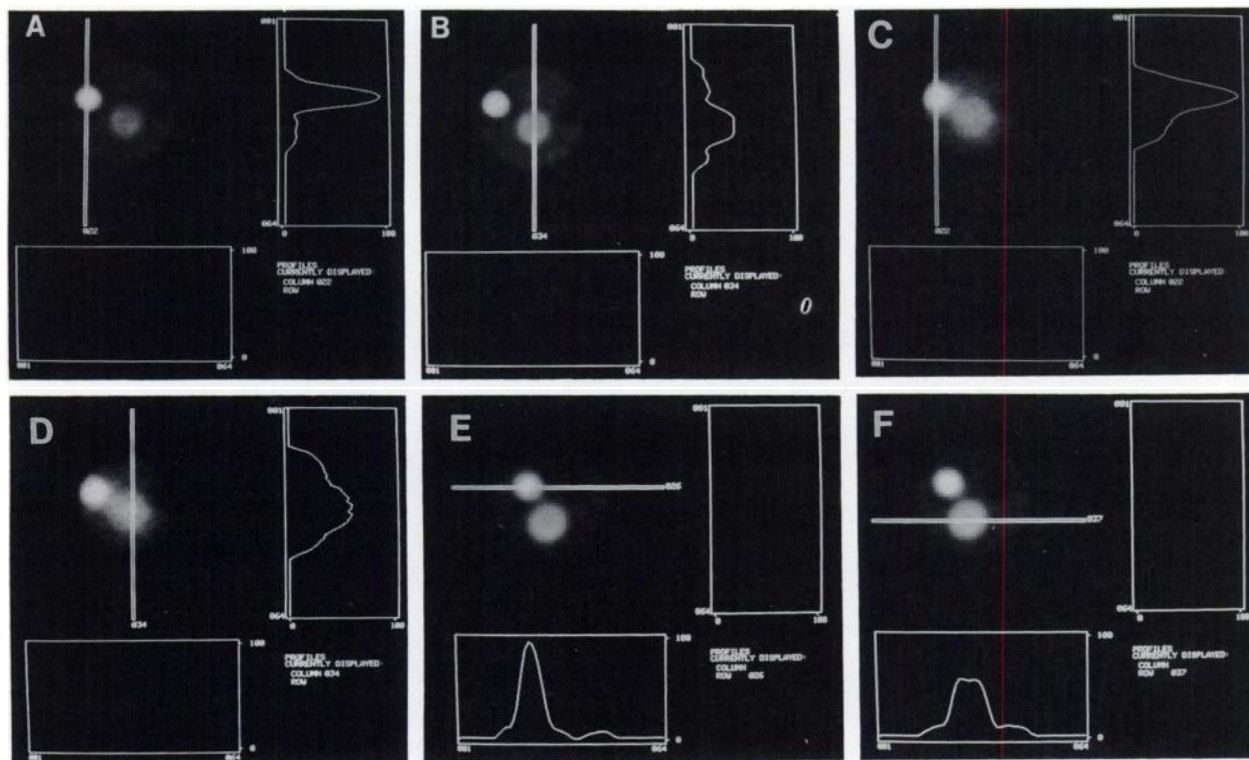
FIGURE 5
Representative transverse SPECT slices of nonuniform activity phantom: (A,B) CHT reconstructions for ^{99m}Tc with profiles of containers 2 and 3. (C,D) Results obtained with commercial software for ^{99m}Tc and profiles corresponding to Figures 5A-B. (E,F) Representative profiles of CHT SPECT slice of ^{111}In-nonuniformity phantom.
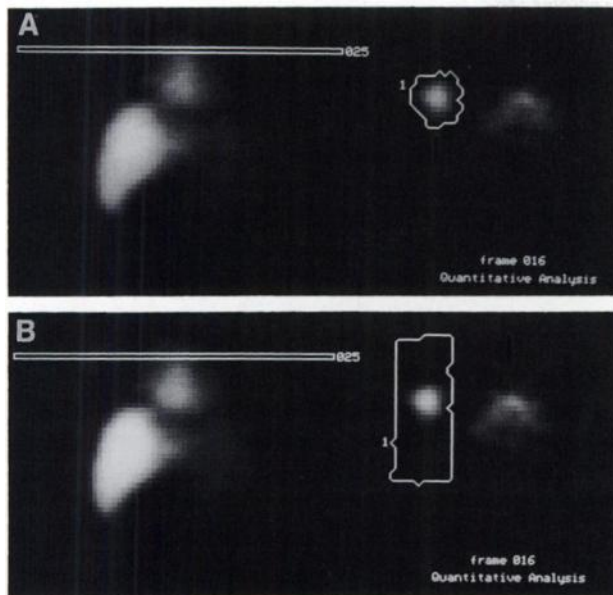
FIGURE 6
CHT SPECT reconstructions and ROI analysis of tumor in patient with Hodgkins disease. Imaging agent was ^{111}In-labeled antiferritin. (A) Typical ROI used with CHT SPECT to determine antibody concentration and dose. (B) ROI analysis of transverse CHT SPECT slice that simulates the ROI corresponding to analysis based on conjugate gamma camera method.

Figure 5 clearly demonstrate that the CHT algorithm and associated software developed by our group are superior to commercial software in resolving hot and cold lesions. Additionally, we analyzed the reconstructed SPECT slices to obtain results for the regional quantitation of nonuniform activity distributions. In analyzing the SPECT data, ROI software was used to determine the total number of counts in each region in individual slices. The regional activity was then obtained by summing over all slices. The gain factor was used to convert counts/voxel to μCi/ml. The results are summarized in Table 2 for ^{99m}Tc and Table 3 for [111]In.

For comparison to accepted clinical practice, we see in Table 4 that CHT SPECT compares favorably to the conjugate view method. This study also underscores the unreliability of the conjugate view method for determining activity in small lesions.

TABLE 1
SPECT Volumetric Phantom Study

Organ	Actual Volume (cc)	SPECT Volume (cc)	% Diff.
Liver	1960	1953	−0.36
Stomach	560	583	+4.1
Spleen	250	246	−1.6
Left Kidney	160	149	−6.9
Pancreas	145	143	−1.4

TABLE 2
Quantitation of Nonuniform Activity Distributions with the CHT SPECT Reconstruction Algorithm for [99m]Tc

Region	Actual concentration (μCi/ml)	Computed concentration (μCi/ml)	% Diff.
Hot (125 ml)	8.00	7.38	−7.7
Medium (500 ml)	3.85	3.78	−1.7
Cold (125 ml)	0	0.46	—
Background	1.28	1.30	+1.5

Total activity was used as a calibration factor; Counts/sinogram: 840K.

Determination of RMS Error in Uniform Cross-Sections

Budinger et al. derived a semi-empirical formula for the RMS error to be expected from a SPECT reconstruction of a uniform concentration of radionuclide (21, 22). In both the ^{99m}Tc and ^{111}In nonuniform bottle studies, several slices of 500k counts/sinogram were close to uniform in concentration. Seed-pixel thresholding was used to obtain an ROI representing a region of uniform concentration from a reconstructed slice of nearly uniform concentration.

From the ^{99m}Tc study, we obtained an RMS error of 0.0784, whereas the approach in Reference 21 indicated that we should expect an RMS error of 0.2675. From the ^{111}In study, the RMS errors were 0.0967 and 0.31357 for the actual and expected RMS errors, respectively. Thus, for studies in this count range, the protocol combined with the CHT algorithm yields about a factor of three improvement in the RMS error.

DISCUSSION AND CONCLUSION

Although the CHT algorithm is computationally more complex than codes based on backprojection, it is a noniterative algorithm that is vectorizable for array processor applications, thus lending itself to rapid calculation in its present form. Of the principal causes of

TABLE 3
Quantitation of Nonuniform Activity Distributions with the CHT SPECT Reconstruction Algorithm for [111]In

Region	Actual concentration (μCi/ml)	Computed concentration (μCi/ml)	% Diff.
Hot (125 ml)	6.57	5.78	−12.0
Medium (500 ml)	4.18	4.10	−2.0
Cold (125 ml)	0	0.18	—
Background	0.60	0.62	+3.1

Estimate of total activity based on calibration of gain factor: 6.42 mCi. Radioassay of total activity: 6.3 mCi. Percent difference: 1.8%. Counts/sinogram: 860K.

TABLE 4
Clinical Comparison: Conjugate Planar View Method and CHT SPECT

Conjugate View Method estimated activity in lesion	64.3 mCi
CHT SPECT ROI analysis simulating Conjugate View Method	57.5 mCi
CHT SPECT ROI analysis of lesion	24.4 mCi

signal degradation in SPECT, attenuation and poor photon statistics are the most important. By exploiting the EDR of the CHT-FT of the sinogram, we are able to minimize the effects of both attenuation and poor statistics. Scatter and poor collimator resolution are significant sources of degradation as well, but the EDR also minimizes these effects, so that it is relatively easy to remove these sources of degradation with the restoration filter. Optimization of the reconstruction protocol required careful analysis of the line source data and a high level of quality control in image acquisition.

The results established by a regional quantification of nonuniform activities are (1) the determination of a gain factor from which one can quantify subsequent tomographic studies, and (2) the accuracy with which the algorithm can determine the unknowns. For phantom studies, these results are adequate for either regional or voxel quantitation. Patient scans are subject to motion artifacts, but are not characterized by large and discontinuous variations in the concentration gradient that are typical of phantom studies. Preliminary results with CHT reconstruction of patient data indicate that the protocol will be useful in the quantitation of radiolabeled antibody activities in tumors and normal organs, and will thereby result in significant improvements in the dosimetry of radiolabeled cancer therapy agents.

APPENDIX

The Energy-Distance Relation and Application to the CHT Algorithm

This discussion is based on the notation and theorems given in Reference 1. For uniform attenuation within a convex body, the SPECT projections are given by:

$$f(p, \phi) = \exp((\mu b(p, \phi)) \int \int_{R_2} g(r, \theta)$$

$$\exp(-\mu r \sin(\theta - \phi)) \delta(p - r\cos(\theta - \phi)) \, r \, dr \, d\theta,$$

where δ is the delta function, and R^2 is the two-dimensional plane. The function b is based on the directed distance from the p-axis to the body contour (Figure 7). The first step in the CHT algorithm is the pre-multiply step that removes the effect of the body contour:

$$P(p, \phi) = \exp(-\mu b) \, f(p, \phi) \qquad \text{(A-1)}$$

The exponential term can be either amplifying or attenuating, depending on the sign of b. The CHT-FT of the sinogram is defined by:

$$\tilde{P}_n(w) = \int_{-\pi}^{\pi} \int_{-\infty}^{\infty} P(p, \phi) \exp(-in\phi - i2\pi wp) \, dp \, d\phi \qquad \text{(A-2)}$$

The Energy-Distance Relation

It is easier to understand the EDR from a geometrical rather than analytical point of view (Fig. 7A). The lines of constant phase of the exponential function of Equation A-2 are shown superimposed on the sinogram of a point source at a distance r_0 from the center of rotation.

The principle of stationary phase tells us that the largest contribution to the integral (Equation A-2) occurs along curves where the imaginary part of the exponential is constant. For fixed (n,w), these curves are lines given by:

$$n\phi + 2\pi wp = \text{const.} \qquad \text{(A-3)}$$

For consistency with the scan-orientation used throughout this article, the source point of (Fig. 7A) is nearest the camera at $\phi = 0$, and farthest away at $\phi = \pi$. The greatest contribution
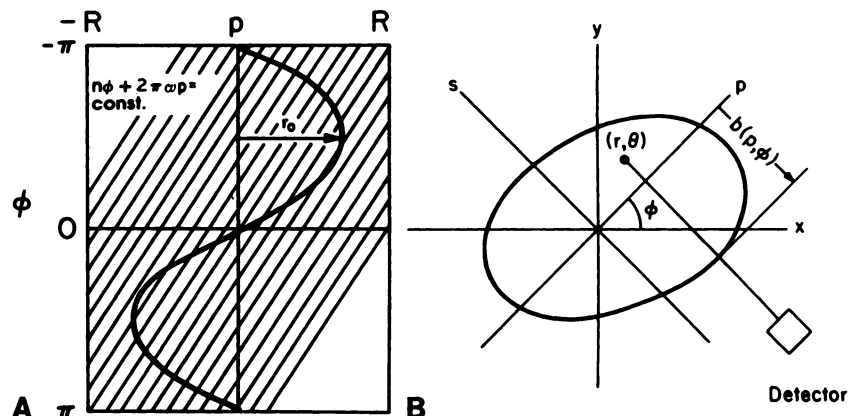
FIGURE 7
(A) Sinogram of a point source located at distance r_0 from the center-of-rotation. Superimposed on the sinogram are the lines of constant phase of the two-dimensional Fourier integral of the pre-multiplied projections. (B) SPECT scanning geometry.

to (Equation A-2), the near-field signal, is for n and w that satisfy:

$$n = +2\pi r_0 w.$$

The far-field signal is concentrated along the ray:

$$n = -2\pi r_0 w,$$

with non-negligible but small contributions from lines of constant phase that are tangent to the curvilinear parts of the sinogram. When the lines of constant phase are not tangent to any part of the sinogram, we would expect a negligible contribution to (Equation A-2) and that is the case.

From a geometrical approach alone, we see that the signal energy of the point source should be concentrated in the bowtie region of the n-w plane:

$$|n| < 2\pi r_0 |w|$$

More rigorous analyses in (6) and (1) yield the same result.

Thus, the energy concentration along the line (Equation A-3) is directly related to the distance of the point-source from the center of rotation. Notice that this result does not depend on the angular coordinate of the point source.

The stationary phase principle is an approximation that holds only in the limit as

$$|n|, |w| \rightarrow \infty.$$

But for n and w commensurate with actual SPECT, it is often a good approximation. However, we do not need actually to make use of approximation. We *can* use the physical interpretation provided by the EDR to improve the signal-to-noise ratio of the CHT algorithm.

The Development of the CHT Algorithm

From Equation A-2 we continue with the outline of the CHT algorithm. The CHT of the object is:

$$g_n(r) = \int_{-\pi}^{\pi} g(r, \theta) \exp(-in\theta) \, d\theta$$

for a discrete set of projection data, consisting of N projections of planar images of size MXM. It was shown that the tomographic slice is reconstructed by:

$$g(r_k, \theta_j) = \sum_{n=-N/2+1}^{N/2} \exp(in\theta_j)$$
$$\times \sum_{m=-M/2+1}^{M/2} \tilde{c}_g(w_m)\tilde{P}_n(w_m)A_n(w_m,r_k) \, \Delta w, \quad (A-4)$$

where $\tilde{c}_g$ is the generalized ramp filter for the intrinsic algorithm (1,2) and the A_ns are related to the eigen functions of the generalized Hankel transform. The quantity Δw is the spatial frequency increment. The A_ns are precomputed and stored as a table. We can regard the summation over m as an inversion matrix for the circular harmonics $g_n(r)$.

Application of the EDR to the CHT Algorithm

We can prove the following identity (1):

$$\left(\frac{t + \mu}{t - \mu}\right)^{n/2} \tilde{P}_n(-t) = (-)^n \left(\frac{t - \mu}{t + \mu}\right)^{n/2} \tilde{P}_n(t)$$

Embedded in this identity is the EDR. For $t \geq \mu$, and $n > 0$,

$\tilde{P}_n(-t)$ is from the far field and is multiplied by a weight greater than one, and $\tilde{P}_n(t)$ is from the near-field and is multiplied by a weight less than one. The noise power of $\tilde{P}_n$ is to a first approximation essentially uniform, since P consists of pixel-by-pixel scalings of mutually independent Poisson random variables. This was checked by Monte Carlo simulations of the noise power spectrum of $\tilde{P}_n$. Therefore, the magnitude of $\tilde{P}_n(-t)$ is more contaminated with noise than $\tilde{P}_n(t)$.

So the quantity:

$$\left(\frac{2\pi w + \mu}{2\pi w - \mu}\right)^{n/2} \tilde{P}_n(-2\pi w)$$

is replaced with:

$$\left(\frac{2\pi w - \mu}{2\pi w + \mu}\right)^n |\tilde{P}_n(2\pi w)| \exp\left(\frac{\tilde{P}(-2\pi w)}{|\tilde{P}_n(-2\pi w)|}\right) \quad (A-5)$$

in the reconstruction of Equation A-4.

The modified CHT based on expression in Equation A-5 is still an exact solution, but has improved noise suppression that was directly measured in both mathematical simulations and phantom studies. We obtain reconstruction of the object by using the inverse FT on the g_ns. The object g is specified for points evenly spaced on a polar grid. Interpolation, or image conversion, is used to obtain an object in rectangular coordinates.

ACKNOWLEDGMENTS

REFERENCES

1. Hawkins WG, Leichner PK, and Yang N-C. The circular harmonic transform for SPECT and boundary conditions on the Fourier transform of the sinogram. *IEEE Trans MI* 1988;7:135–148.
2. Gullberg GT, Budinger TF. The use of filtering methods to compensate for constant attenuation in single-photon computed tomography. *IEEE Trans Biomed Eng* 1981;28:142–157.
3. Tretiak OJ, Metz C. The exponential radon transform. *Siam J Appl Math* 1980;39:341–354.
4. Bellini S, Piacenti M, Cafforio C, and Rocca F. Compensation of tissue absorption in emission tomography. *IEEE Trans ASSP* 1979;27:213–218.
5. Hawkins WG, Barrett HH. A numerically stable circular harmonic reconstruction algorithm. *Siam J Numer Analy* 1986;23:873–890.
6. Edholm PR, Lewitt RM, Lindholm B. Novel properties of the Fourier decomposition of the sinogram. *SPIE Proc* 1986;671:8–18.
7. Lewitt RM, Edholm PR, and Xia W. Fourier method for correction of depth-dependent collimator blurring. *SPIE Medical Image Processing III. Image Processing* 1989;1092:232–243.
8. King MA, Doherty PW, Schwinger RB. A Wiener filter for nuclear medicine images. *Med Phys* 1983;10:876–880.
9. Goodman JW, Belchner JF. Fundamental limitations in the linear invariant restoration of atmospherically-degraded images in imaging through the atmosphere. *SPIE* 1976;75:141–154.

10. Helstrom CW. Image restoration by the method of least squares. *J Opt Soc Am* 1967;57:296–303.
11. Floyd CE, Jaszczak RJ, Greer KL, Coleman RE. Deconvolution of Compton scatter in SPECT. *J Nucl Med* 1985;26:403–408.
12. Oppenheim E, Appledorn CR. Uniformity correction for SPECT using a mapped colbalt-57 sheet source. *J Nucl Med* 1985;26:409–415.
13. Jaszczak RJ, Chang LT, Stein NA, Moore FE. Whole body single-photon emission computed tomography using dual, large-field-of-view scintillation cameras. *Phys Med Biol* 1979;24:1123–1143.
14. Cormack AM. Reconstruction of densities from their projections with applications in radiological physics. *Phys Med Biol* 1973;18:195–207.
15. Todd-Pokropek AE, Jarritt PH. In: Ell PJ, Holman BL, eds., *The noise characteristics of SPECT systems in computed emission tomography.* Oxford: Oxford University Press; 1982:361–389.
16. Metz CE, Doi K. Transfer function analysis of radiographic imaging systems. *Phys Med Biol* 1979;24:1079–1106.
17. Leichner PK, Klein JL, Siegelman SS, et al. Dosimetry of I-131 labeled antiferritin in hepatoma: Specific activities in the tumor and liver. *Cancer Treat Rep* 1983;67:647–657.
18. Leichner PK, Yang N-C, Frenkel TL, et al. Dosimetry and treatment planning for Y-90 labeled antiferritin in hepatoma. *Int J Radiat Oncol Biol Phys* 1988;14:1033–1042.
19. Thomas SR, Maxon HR, Keriakes HG. In-vivo quantitation of lesion radioactivity using external counting methods. *Med Phys* 1976;3:253–255.
20. Hammond ND, Moldofsky PJ, Beardsley MR, et al. External imaging techniques for quantitation of distribution of I-131 (f(ab')2) fragments of monoclonal antibodies in humans. *Med Phys* 1984;11:778–783.
21. Budinger TF, Gullberg GT, Huesman RH. Emission computed tomography. In: Herman GT, ed. *Topics in applied physics: image reconstruction from projections.* New York: Springer-Verlag; 1979:147–242.
22. Barrett HH, Gordon SK, Hershel RS. Statistical limitations in transaxial tomography. *Comp Biol Med* 1976;6:307–323.
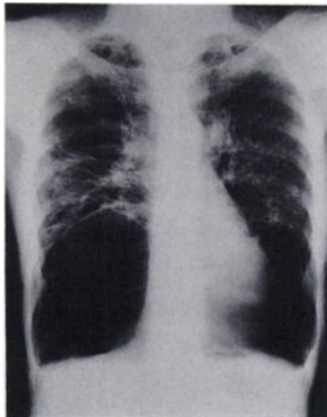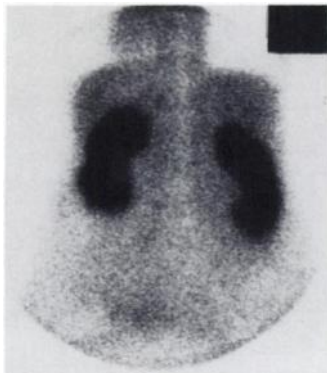
FIRST IMPRESSIONS

PURPOSE:
A 56-yr-old woman with bilateral renal calculi was referred for baseline preoperative assessment. On the posterior renal image, there was good tracer uptake by the kidneys, however, the lung fields were strikingly photopenic. CXR correlation revealed large bullae at the lung bases. The only known predisposing factor at the time of this study was a history of cigarette smoking.

TRACER:
600 MBq of ^{99m}Tc-DTPA

ROUTE OF ADMINISTRATION:
Intravenous injection

TIME AFTER INJECTION:
4 minutes

INSTRUMENTATION:
LFOV gamma camera with a high-resolution collimator

CONTRIBUTORS:
K.K.L. Choong and S.M. Gruenewald

INSTITUTION:
Westmead Hospital, Sydney, Australia